

# Theoretical analysis of modulation doping effects on intersubband transition properties of semipolar AlGaN/GaN quantum well

Houqiang Fu, Hong Chen, Xuanqi Huang, Zhijian Lu, and Yuji Zhao

Citation: *J. Appl. Phys.* **121**, 014501 (2017); doi: 10.1063/1.4972975

View online: <http://dx.doi.org/10.1063/1.4972975>

View Table of Contents: <http://aip.scitation.org/toc/jap/121/1>

Published by the [American Institute of Physics](#)

---

## Articles you may be interested in

[Carrier localization in the vicinity of dislocations in InGaN](#)

*J. Appl. Phys.* **121**, 013104013104 (2017); 10.1063/1.4973278

[Investigation of the light-extraction efficiency in 280 nm AlGaIn-based light-emitting diodes having a highly transparent p-AlGaIn layer](#)

*J. Appl. Phys.* **121**, 013105013105 (2017); 10.1063/1.4973493

[Nanoscale visualization of electronic properties of Al<sub>x</sub>Ga<sub>1-x</sub>N/Al<sub>y</sub>Ga<sub>1-y</sub>N multiple quantum-well heterostructure by spreading resistance microscopy](#)

*J. Appl. Phys.* **121**, 014305014305 (2017); 10.1063/1.4973306

[The effect of polarity on MOCVD growth of thick InGaIn](#)

*J. Appl. Phys.* **110**, 022101022101 (2017); 10.1063/1.4972967

---

**AIP** | Journal of  
Applied Physics

**INTRODUCING INVITED PERSPECTIVES**

**Ultrafast magnetism and THz spintronics**

Authors: Jakob Walowski and Markus Münzenberg

# Theoretical analysis of modulation doping effects on intersubband transition properties of semipolar AlGaIn/GaN quantum well

Houqiang Fu, Hong Chen, Xuanqi Huang, Zhijian Lu, and Yuji Zhao  
 School of Electrical, Computer and Energy Engineering, Arizona State University, Tempe,  
 Arizona 85287, USA

(Received 7 September 2016; accepted 12 December 2016; published online 3 January 2017)

The effects of modulation doping on the intersubband transition (ISBT) properties of semipolar AlGaIn/GaN quantum well (QW) are investigated theoretically using QW doping, barrier doping, and barrier  $\delta$ -doping schemes at 150 K. Important ISBT parameters such as intersubband transition energies, dipole matrix elements, and absorption spectra are calculated for QW structures on both semipolar (20 $\bar{2}$ 1) (i.e., with weak polarization) and (10 $\bar{1}$ 3) (i.e., with strong polarization) planes. For (20 $\bar{2}$ 1) QW with weak polarization, it is found that high doping concentrations can cause a significant band bowing to the QW structures, which reduce the absorption coefficients and wavelengths. This band bowing effect will become stronger when doping layers are closer to the QW. For (10 $\bar{1}$ 3) QW with a strong polarization, however, a weak band bowing effect is observed due to the large polarization and large band tilting of (10 $\bar{1}$ 3) QW. The study shows that modulation doping is a promising method to modify the ISBT properties of semipolar AlGaIn/GaN QW to achieve an improved performance such as longer ISBT wavelength (e.g., >20  $\mu$ m).  
 Published by AIP Publishing. [<http://dx.doi.org/10.1063/1.4972975>]

## I. INTRODUCTION

III-nitride semiconductors including GaN, AlN, InN, and their alloys enable high performance visible light-emitting diodes and laser diodes for solid-state lighting and display applications.<sup>1–4</sup> Due to their excellent material properties such as large longitudinal optical phonon energy ( $\sim 90$  meV), large band offset ( $\sim 2$  eV for GaN/AlN) and ultrafast carrier dynamics ( $\sim 100$  fs),<sup>5,6</sup> III-nitride materials are also attractive for various intersubband transition (ISBT) devices and applications including quantum well infrared photodetectors (QWIPs),<sup>7</sup> quantum cascade lasers (QCLs),<sup>5</sup> and quantum cascade detectors (QCDs).<sup>8</sup> One of the major technical issues for the design and fabrication of ISBT devices is the required high doping concentration ( $>10^{18}$  cm<sup>-3</sup>) in the quantum well (QW), which will degrade the material quality and increase the impurity scattering.<sup>9,10</sup> Furthermore, the heavy doping in the QW are also detrimental to the ISBT properties such as the transition energy linewidth and absorption coefficient, due to the bandstructure change and many-body effects including depolarization, excitonic shifts, and exchange term.<sup>10–12</sup> Helman *et al.* observed absorption wavelength blueshift in doped GaN/InGaIn QWs compared to undoped structures due to many-body effects.<sup>10</sup> Kandaswamy *et al.* found that increasing doping concentration could result in more than 50% of energy separation of first two subbands.<sup>11</sup> Alternatively, modulation doping such as  $\delta$ -doping has been proposed as a promising method for the fabrication of high performance ISBT devices.<sup>13</sup> Unlike the conventional doping method, the modulation doping will spatially separate the electron in the QW from the impurities in the barrier, leading to advantageous properties such as high doping concentration, higher electron mobility, and narrower absorption linewidth and suppressed many-body effects.<sup>9–12</sup>

Recently, QW based on nonpolar and semipolar III-nitride materials have emerged as new ISBT structures with improved device performance.<sup>6,14–18</sup> One major drawback for conventional polar *c*-plane III-nitride ISBT devices is the large polarization inside the QW, which leads to a quantum-confined Stark effect (QCSE) and a tilted QW profile. As a result, the wavelength of the *c*-plane III-nitride ISBT device is limited.<sup>19,20</sup> In contrast, nonpolar and semipolar III-nitride QWs can have much reduced polarizations depending on the crystal orientations,<sup>21–27</sup> and improved ISBT performance such as transition energies and absorption coefficients are reported on semipolar QWs.<sup>16,17,28</sup> Our previous work showed that semipolar planes with an inclination angle larger than 55° from *c*-plane are promising candidates for terahertz (THz) optoelectronics.<sup>18</sup> Despite these progresses, the doping characteristics and their effects on the semipolar QW ISBT devices have never been explored.

In this work, we theoretically investigate the modulation-doping induced band bowing effects on the ISBT properties of AlGaIn/GaN QW structures on semipolar (20 $\bar{2}$ 1) plane (with weak polarization) and (10 $\bar{1}$ 3) plane (with strong polarization) at 150 K, where conventional QW doping scheme is also studied as reference. Very distinct phenomena have been observed for two structures: for (20 $\bar{2}$ 1) single quantum well (SQW) with weak polarization, it is found that high doping concentrations can cause significant band bowing to the QW structure, which reduce the absorption coefficients and wavelengths. This band bowing effect will become stronger when the doping layers are closer to the QW. For (10 $\bar{1}$ 3) QW with a strong polarization, however, a weak band bowing effect is observed due to large polarization and large band tilting of (10 $\bar{1}$ 3) QW. The study shows that modulation doping is a promising method to modify the ISBT properties of semipolar AlGaIn/GaN QW to achieve

an improved performance such as longer ISBT wavelength (e.g.,  $>20 \mu\text{m}$ ).

## II. SIMULATION METHODS

The ISBT properties of AlGaIn/GaN SQW are studied on two semipolar planes where  $(10\bar{1}3)$  plane has a strong polarization while  $(20\bar{2}1)$  plane has a weak polarization. All the structures in the simulation contain a 30 nm  $\text{Al}_{0.35}\text{Ga}_{0.65}\text{N}$  barrier and a 12 nm GaN QW. The aluminum (Al) composition is similar to that of the typical GaAs based ISBT devices.<sup>6</sup> It should be noted that the thickness of the high Al composition barrier is close to the critical thickness, which might be challenging for barrier growth. The effect of barrier thickness on ISBT properties is discussed in Ref. 18. Three doping schemes are implemented on these structures: QW doping, barrier continuous doping (referred as barrier doping), and barrier  $\delta$ -doping (referred as  $\delta$ -doping), which are shown schematically in Fig. 1. The doping concentrations and positions are varied to explore the doping effects on the ISBT properties. Table I summarizes device structures simulated in the paper. The commercial software SiLENSE developed by STR group is utilized to calculate the bandstructures, subband wavefunctions, subband electron densities, and dipole matrix elements, which has been widely used in III-nitride optoelectronic studies.<sup>6,29</sup> More details about the software can be found in Ref. 30. In the software, one-dimensional Schrödinger-Poisson equation is solved self-consistently with a drift-diffusion model included. The simulation includes the effects of strain and polarization for arbitrary crystal orientations of III-nitride materials, which are critical for III-nitride optoelectronic devices. The material properties including the elastic constants and piezoelectric coefficients that the software used are listed in Table II.

The polarization of semipolar AlGaIn/GaN heterostructure is calculated using a method proposed by Romanov *et al.* where the analytical formalism in linear elasticity is incorporated.<sup>21</sup> The primed coordinate  $z'$  is along the normal to the epilayers and  $x'$  and  $y'$  are in the substrate surface plane. The lattice constant of AlGaIn is obtained according

to the Vegard law. For a semipolar plane titled from  $c$ -plane by an angle of  $\theta$ , the total polarization difference along  $z'$  at AlGaIn/GaN interface can be expressed as a function of  $\theta$  by<sup>21</sup>

$$P_{tot} = P_{pz}^{\text{GaIn}} + (P_{sp}^{\text{GaIn}} - P_{sp}^{\text{AlGaIn}}) \cos \theta, \quad (1)$$

where  $P_{tot}$  is the total polarization difference between AlGaIn barrier and GaN QW, and  $P_{sp}^{\text{AlGaIn}}$  and  $P_{sp}^{\text{GaIn}}$  are the spontaneous polarization of AlGaIn barrier and GaN QW, respectively.  $P_{pz}^{\text{GaIn}}$  is the strain-induced piezoelectric polarization in the GaN layer, which is expressed as<sup>21,31</sup>

$$P_{pz}^{\text{GaIn}} = e_{31} \cos \theta \epsilon_{x'x'} + \left( e_{31} \cos^3 \theta + \frac{e_{33} - e_{15}}{2} \sin \theta \sin 2\theta \right) \epsilon_{y'y'} + \left( \frac{(e_{31} + e_{15})}{2} \sin \theta \sin 2\theta + e_{33} \cos^3 \theta \right) \epsilon_{z'z'} + [(e_{31} - e_{33}) \cos \theta \sin 2\theta + e_{15} \sin \theta \cos 2\theta] \epsilon_{y'z'}, \quad (2)$$

where elements  $\epsilon_{k'l'}$  are the strain tensor components and elements  $e_{ij}$  are the components of piezoelectric tensor in Voigt notation. The polarization (absolute value) of  $(10\bar{1}3)$  plane is larger than the  $(20\bar{2}1)$  plane. The simulation results obtained in SiLENSE are fed into the MATLAB code to calculate the ISBT absorption spectra, which is expressed as the following:<sup>9,32</sup>

$$\alpha(\lambda) = \frac{8\pi^3 c^2 \mu}{\lambda n_r L} |M_{12}|^2 n_{12} \frac{h/(2\pi\tau)}{(E_2 - E_1 - hc/\lambda)^2 + [h/(2\pi\tau)]^2}, \quad (3)$$

where  $\alpha(\lambda)$  is the ISBT absorption coefficient between the first two subbands,  $L$  is the QW thickness,  $c$  is the speed of light in vacuum,  $\mu$  is the permeability of QW material,  $\lambda$  is wavelength of incident light,  $n_r$  is refractive index,  $M_{12}$  is the dipole matrix element of first two subbands,  $n_{12}$  is the difference of electron concentration between the first and the second subband,  $E_1$  is the energy of the first subband,  $E_2$  is the energy of the second subband, and  $\tau$  is the

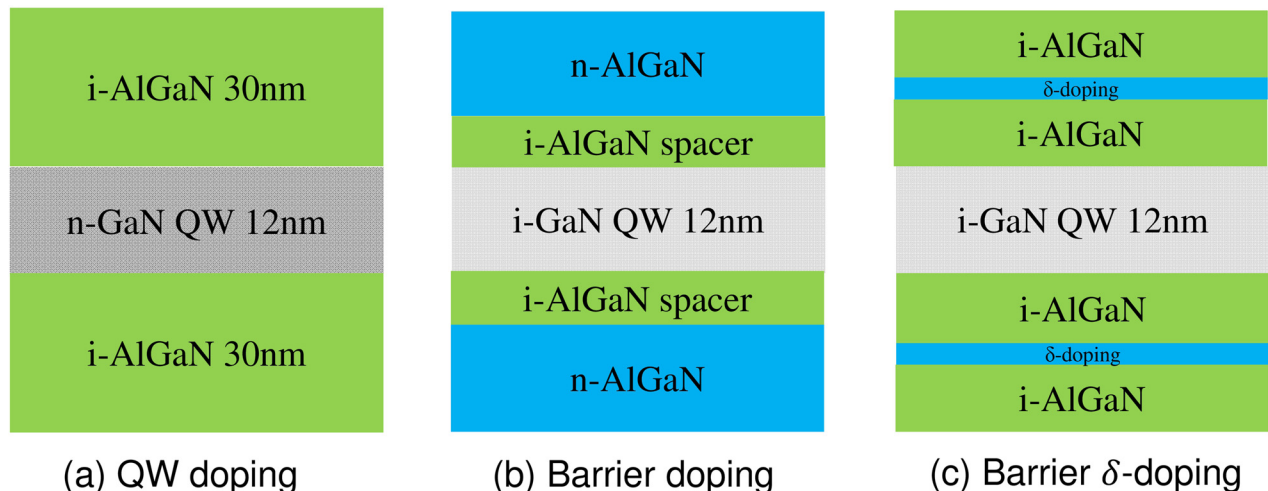


FIG. 1. Schematics of three different doping schemes: (a) QW doping; (b) barrier doping, and (c) barrier  $\delta$ -doping. In (b), the thickness of the undoped AlGaIn spacer layer can be varied. In (c), the position of  $\delta$ -doping can be changed.

TABLE I. Simulated device structures and doping schemes.

	(10 $\bar{1}$ 3) QW structure	(20 $\bar{2}$ 1) QW structure
Inclination angles from <i>c</i> -plane <sup>26</sup>	32°	75°
QW layer	12 nm GaN	12 nm GaN
Barrier layer	30 nm Al <sub>0.35</sub> Ga <sub>0.65</sub> N	30 nm Al <sub>0.35</sub> Ga <sub>0.65</sub> N
QW doping	Doping: $3 \times 10^{18}$ – $1 \times 10^{19}$ cm <sup>-3</sup>	Doping: $3 \times 10^{18}$ – $1 \times 10^{19}$ cm <sup>-3</sup>
Barrier doping	Doping: $3 \times 10^{18}$ – $1 \times 10^{19}$ cm <sup>-3</sup> Spacer thickness: 0–10 nm	Doping: $3 \times 10^{18}$ – $1 \times 10^{19}$ cm <sup>-3</sup> Spacer thickness: 0–10 nm
$\delta$ -doping	Doping: $2 \times 10^{12}$ – $1 \times 10^{13}$ cm <sup>-2</sup> Position: 2–10 nm	Doping: $2 \times 10^{12}$ – $1 \times 10^{13}$ cm <sup>-2</sup> Position: 2–10 nm

relaxation time (60 fs is used<sup>6</sup>). The dipole matrix element  $M_{12}$  is defined as

$$M_{12} = e \int_{-\infty}^{\infty} \psi_2^*(z) z \psi_1(z) dz, \quad (4)$$

where  $e$  is the electron charge,  $z$  is the normal to the epilayer,  $\psi_1$  and  $\psi_2$  are first two subband wavefunctions.  $n_{12} = n_1 - n_2$  where  $n_1$  and  $n_2$  are the electron concentration in the first and second subband, respectively. In a QW system, the electron concentration  $n_i$  of the  $i$ th subband is calculated by the integral of Fermi-Dirac distribution and density of states as the following:

$$n_i = \int_{E_i}^{\infty} \frac{m^*}{\pi \hbar^2} \frac{1}{1 + e^{\frac{E-E_f}{kT}}} dE = \frac{4\pi m^* kT}{h^2} \ln \left( 1 + e^{\frac{E_f-E_i}{kT}} \right), \quad (5)$$

where  $m^*$  is the effect mass,  $k$  is the Boltzmann constant,  $T$  is the operation temperature,  $h$  is the Planck constant,  $E_f$  is the Fermi energy, and  $E_i$  is the energy of  $i$ th subband. In this

TABLE II. Material parameters used in SiLENS software for calculating the conduction band, electron wavefunction, and electron concentration.

Material parameter	Unit	AlN	GaN
Elastic constant $C_{11}$	GPa	395	375
Elastic constant $C_{12}$	GPa	140	140
Elastic constant $C_{13}$	GPa	115	105
Elastic constant $C_{33}$	GPa	385	395
Elastic constant $C_{44}$	GPa	120	100
Piezoelectric coefficient $e_{15}$	C/cm <sup>2</sup>	-0.48	-0.27
Piezoelectric coefficient $e_{31}$	C/cm <sup>2</sup>	-0.58	-0.33
Piezoelectric coefficient $e_{33}$	C/cm <sup>2</sup>	1.55	0.65
$P_{sp}$	C/cm <sup>2</sup>	-0.081	-0.029
Donor ionization energy	meV	13	13
Acceptor ionization energy	meV	470	170
Lattice constant $a$	nm	0.3112	0.3188
Lattice constant $c$	nm	0.4982	0.5186
Energy bandgap	eV	6.25	3.51
Varshni parameter $a$	meV/K	1.80	0.91
Varshni parameter $b$	K	1462	830
Crystal-field splitting	meV	-93	22
Spin-orbital splitting	meV	11	11
Electron affinity	eV	0	1.96
Dielectric constant	...	8.5	8.9
Electron effective mass along axis $a$	$m_0$	0.26	0.2
Electron effective mass along axis $c$	$m_0$	0.25	0.2
Heavy hole effective mass along axis $a$	$m_0$	2.58	1.65
Heavy hole effective mass along axis $a$	$m_0$	1.95	1.1

work, the temperature  $T$  is set as 150 K. Usually, III-nitride ISBT devices are simulated or characterized at low temperature in order to reduce the thermal noise and improve the signal-to-noise ratio.<sup>6,11,16,17</sup> Room temperature operation of III-nitride ISBT devices has not been realized and is undergoing a research topic. The electron effective mass is  $0.2 m_0$  for both semipolar planes since the in-plane anisotropy effect is negligible.

### III. RESULTS AND DISCUSSIONS

Before discussing the ISBT properties of doped QW structures, it is necessary to calculate the bandstructures and subband wavefunctions of (10 $\bar{1}$ 3) and (20 $\bar{2}$ 1) devices with undoped QW and barrier. Figure 2 shows the results of undoped AlGa<sub>0.35</sub>N (30 nm)/GaN (12 nm) QW on (10 $\bar{1}$ 3) and (20 $\bar{2}$ 1) planes. It should be noted that the 200 nm GaN buffer layer is included below the AlGa<sub>0.35</sub>N barrier. Without doping, both the band diagrams show no signs of bowing which is consistent with previous results.<sup>6,18</sup> Furthermore, it is evident that (10 $\bar{1}$ 3) QW has a more tilted QW profile and both larger energy and spatial separation compared with (20 $\bar{2}$ 1) SQW. This will lead to distinct ISBT properties when these semipolar QWs are doped. In Secs. III A - III C, we will compare the three doping schemes for (10 $\bar{1}$ 3) and (20 $\bar{2}$ 1) QWs and identify the optimal doping schemes for best ISTB performance.

#### A. Doping schemes

Figure 1 shows the schematic structures of three doping schemes that are used in this study. QW doping is uniformly doped over the QW layer, which is the most common doping scheme. The other two doping schemes are modulation doping schemes where the QW layer is unintentionally doped ( $10^{15}$  cm<sup>-3</sup>). In order to solely investigate the effect of doping concentrations, the spacer thickness in the barrier doping scheme is maintained at 2 nm, and the position of  $\delta$ -doping is 2 nm away from the barrier/QW interface. The doping concentrations of QW doping and barrier doping schemes are varied from  $3 \times 10^{18}$  to  $1 \times 10^{19}$  cm<sup>-3</sup> while  $\delta$ -doping is increasing from  $2 \times 10^{12}$  to  $1 \times 10^{13}$  cm<sup>-2</sup>. It is noteworthy that  $\delta$ -doping is simulated by doping over 0.5 nm in the barrier, because  $\delta$ -doping is typically spread over a thin layer. Figure 3 shows the absorption spectra of (10 $\bar{1}$ 3) and (20 $\bar{2}$ 1) SQW under the three doping schemes with various doping concentrations. The two devices show a different range of absorption wavelength due to different polar characters of

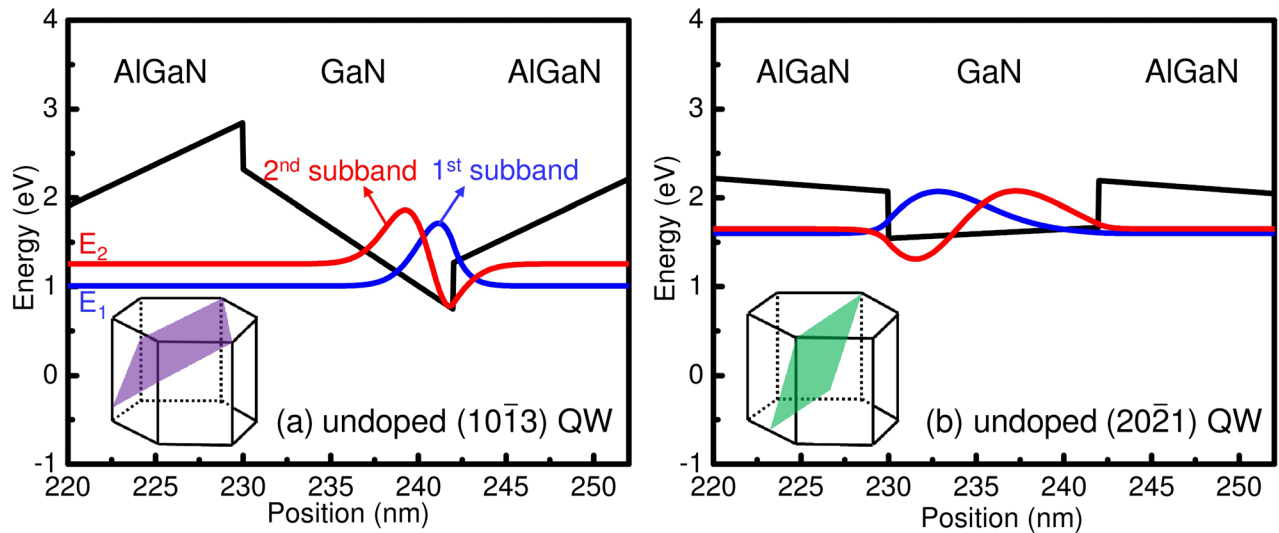


FIG. 2. The conduction band and the electron wavefunctions of first two subbands of undoped AlGaIn (30 nm)/GaN (12 nm) QWs on (a)  $(10\bar{1}3)$  and (b)  $(20\bar{2}1)$  planes. The insets show the schematic view of the two semipolar planes.  $E_1$  and  $E_2$  are energy levels of the first and second subband.

the two crystal planes.<sup>18</sup> It is clear that  $(20\bar{2}1)$  SQW exhibits different tendencies compared to  $(10\bar{1}3)$  structure in terms of peak absorption coefficients and wavelengths when increasing the doping concentrations. Figure 4(a) summarizes the peak wavelengths of the absorption spectra in Fig. 3. For both  $(20\bar{2}1)$  and  $(10\bar{1}3)$  SQW, the peak absorption

wavelengths move towards longer wavelengths with higher doping concentrations under all doping schemes. However, the absorption spectra of  $(10\bar{1}3)$  SQW peaks in the range of 5–8  $\mu\text{m}$  and the increase of peak wavelength is relatively small, which is not desirable for terahertz (THz) or far infrared (FIR) applications. In contrast,  $(20\bar{2}1)$  SQW shows a

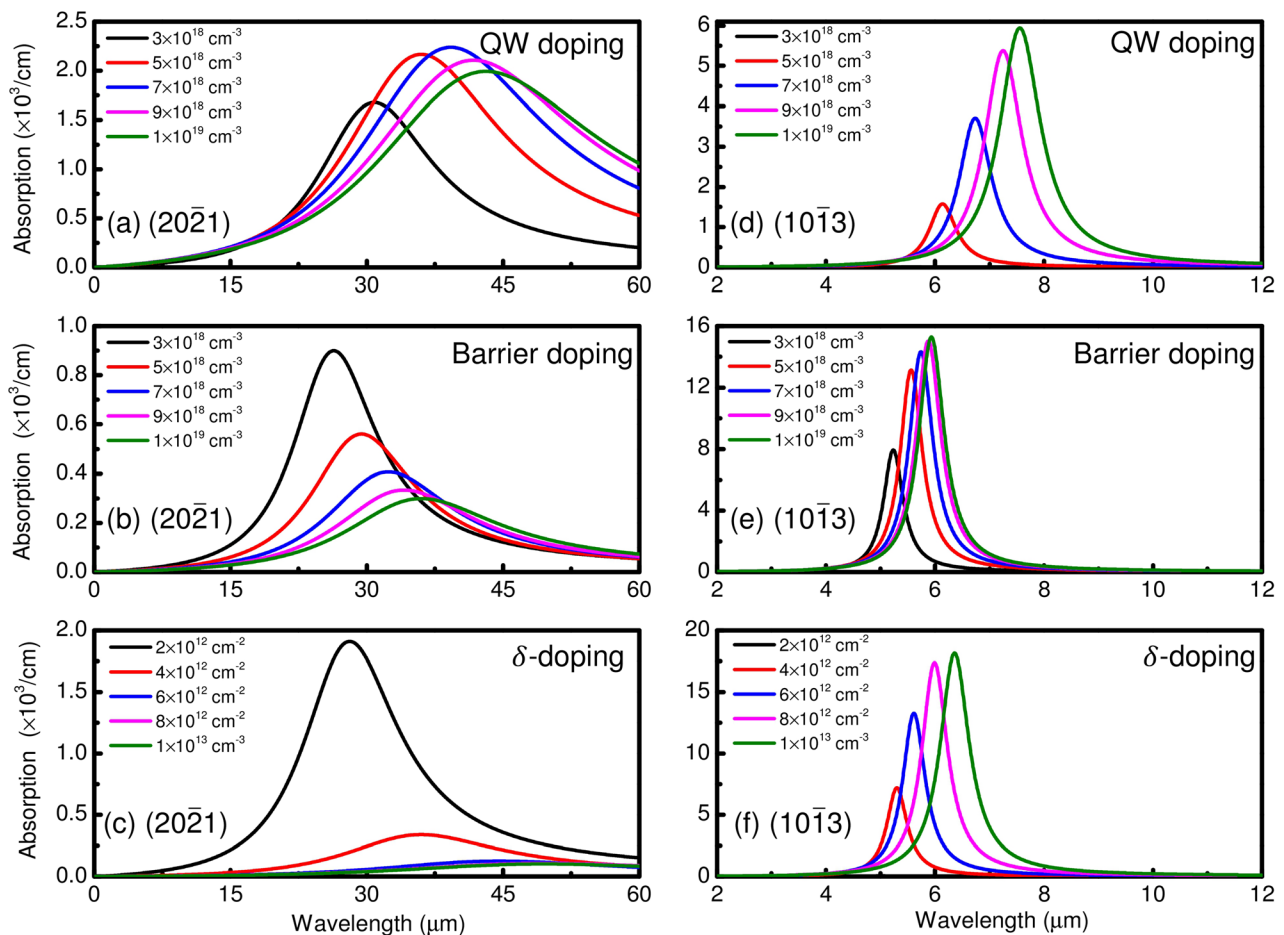


FIG. 3. The absorption spectra of  $(20\bar{2}1)$  QWs with various doping densities under (a) QW doping, (b) barrier doping, and (c)  $\delta$ -doping schemes. The absorption spectra of  $(10\bar{1}3)$  QWs with various doping densities under (d) QW doping, (e) barrier doping, and (f)  $\delta$ -doping schemes.

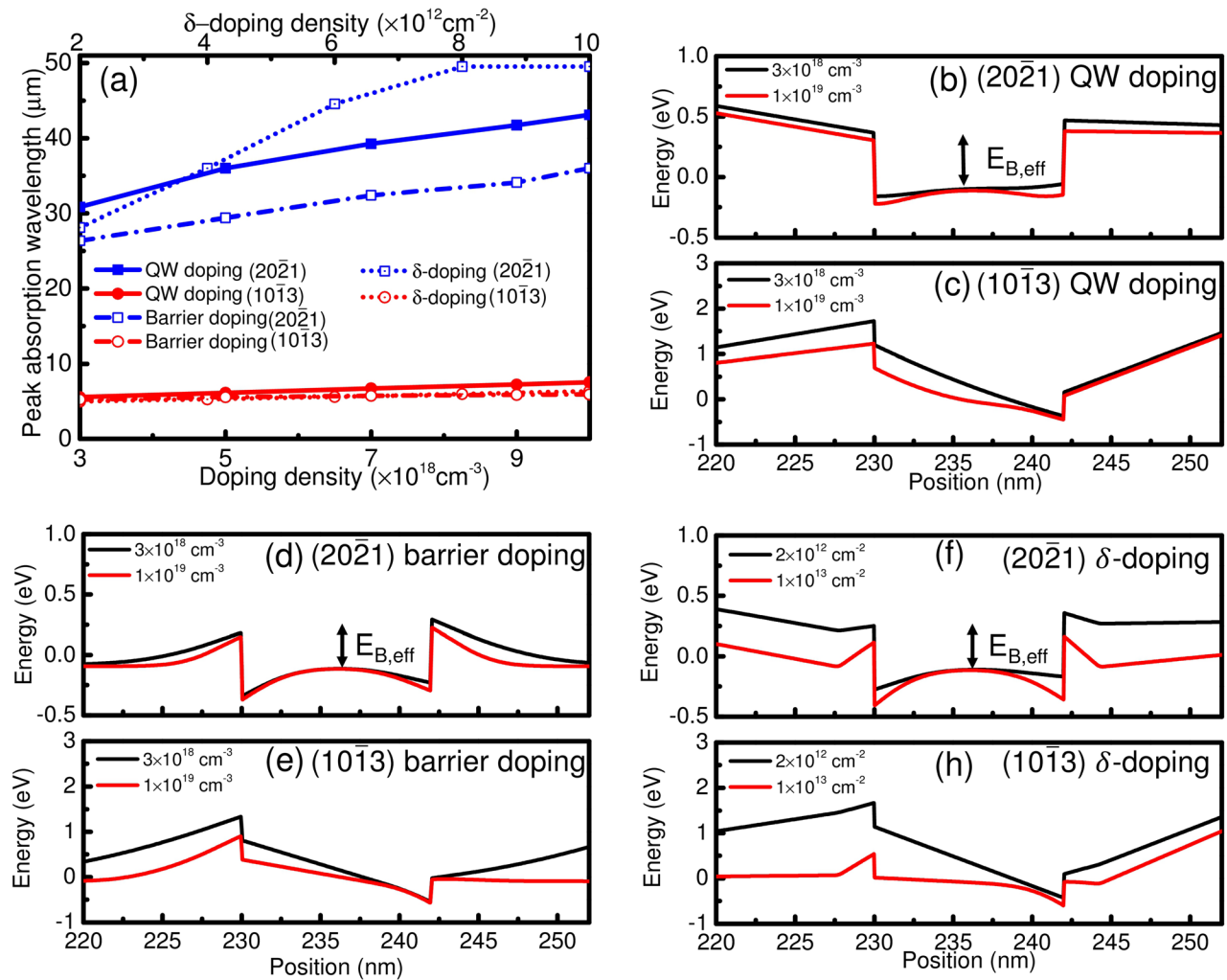


FIG. 4. (a) The peak absorption wavelength as a function of doping density for (2021) and (1013) QWs under three doping schemes. (b)–(h) conduction band of (2021) and (1013) QWs under three doping schemes at high and low doping densities.

large wavelength red shift in the range of 25–50  $\mu\text{m}$  when the doping concentration increases. However, the longer absorption wavelengths at highly doped (2021) devices come with the penalty of reduced peak absorption: modulation doping schemes (barrier doping and  $\delta$ -doping) result in more reduction of absorption than the QW doping scheme. Surprisingly, the peak absorption coefficient of (1013) SQW is increased significantly by a high doping concentration although the wavelength red shift is minimal. In short, (2021) SQW has increased absorption wavelengths but decreased absorption coefficients at high doping concentrations, while an increase in both absorption wavelengths and coefficients are observed on (1013) SQW with increasing doping concentrations.

According to Fig. 4(a), different doping schemes result in a small difference in peak absorption wavelengths for (1013) SQW, while the absorption wavelengths of (2021) SQW show a strong dependence on doping schemes. For (2021) structures in large doping concentration ranges (e.g.,  $>5 \times 10^{18}$ – $10^{19} \text{ cm}^{-3}$ ), the magnitude of peak absorption wavelengths is in the following order:  $\delta$ -doping > QW doping > barrier doping. This verifies the potential implementation of  $\delta$ -doping in long-wavelength devices with additional benefits of reduced

carrier scattering and impurities in the QW layer. Figures 4(b)–4(h) explain the absorption wavelength shift with an increasing doping density for the (2021) and (1013) SQWs under different doping schemes. At high doping concentrations, large bandstructure bowing occurs in the QW layer of (2021) structures. This reduces the effective barrier height  $E_{B,eff}$  and leads to a smaller subband separation in energy, which results in an increased absorption wavelength. (2021) structures under the  $\delta$ -doping scheme show the largest absorption wavelength due to their largest bowing of the QW profile compared with QW profiles under other two doping schemes. On the other hand, the band bending of (1013) SQW is complicated by the combination of polarization charge and the carrier from the doping. Due to the strong polarization at the interface, the right side of the QW profile is pinned, no matter what the doping concentration is. As a result, the bandstructure is bent down at the left side. At high doping concentrations, the resulting bandstructure on (1013) is still tilted which limits the separation of subband wavefunctions. This explains the small variation of absorption wavelength with increasing doping concentration on (1013) structures.

Figures 5(a) and 5(b) present the electron density difference  $n_{12}$  and the matrix element  $M_{12}/e$  as a function of the

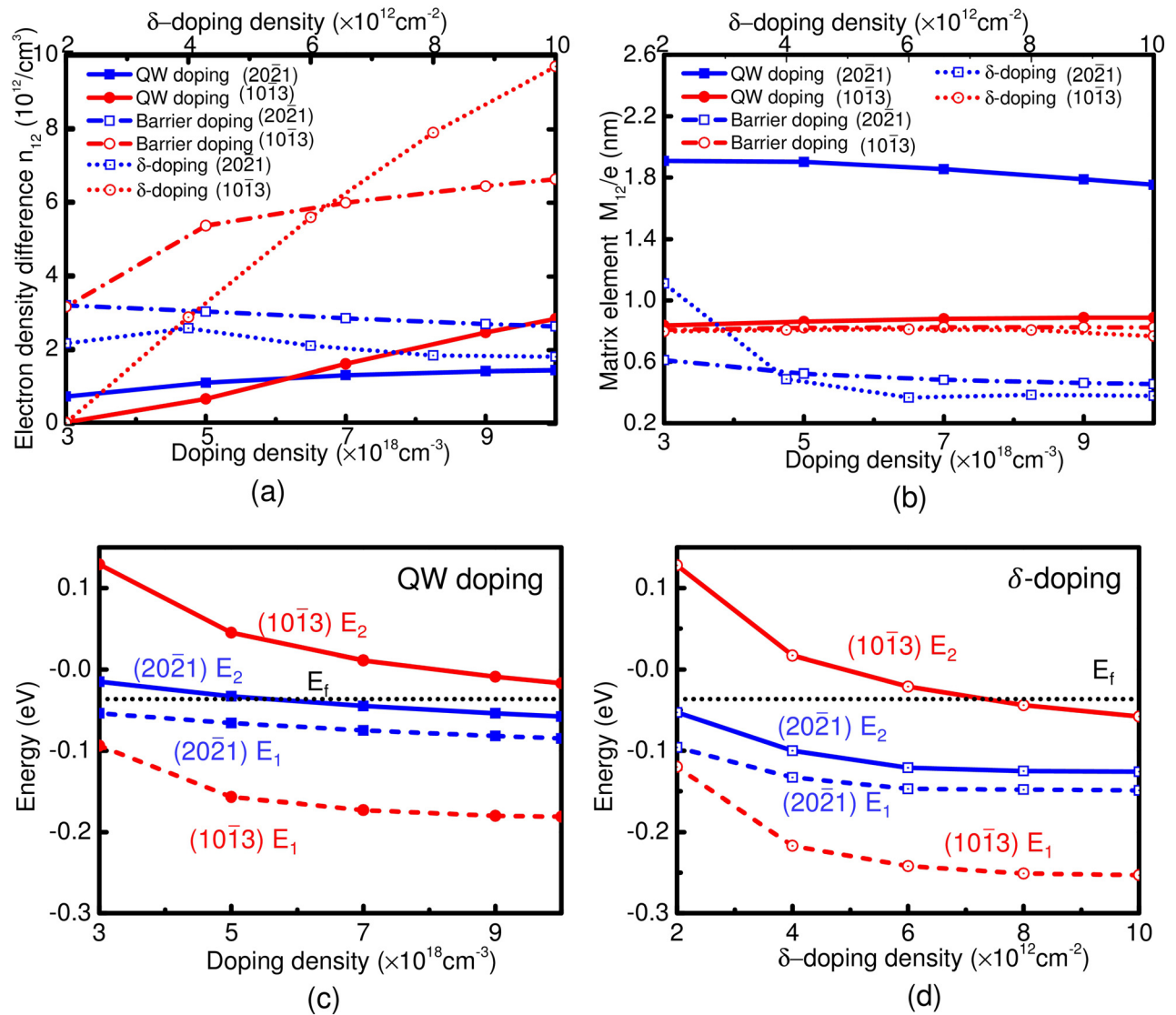


FIG. 5. (a) Electron density difference  $n_{12}$  and (b) matrix element  $M_{12}/e$  versus doping densities for  $(20\bar{2}1)$  and  $(10\bar{1}3)$  QWs under different doping schemes.  $E_1$ ,  $E_2$ , and  $E_f$  for  $(20\bar{2}1)$  and  $(10\bar{1}3)$  QWs under (c) QW doping scheme and (d)  $\delta$ -doping scheme. The results under the barrier doping scheme is not shown due to a similar trend to  $\delta$ -doping scheme.

doping concentrations for  $(20\bar{2}1)$  and  $(10\bar{1}3)$  QWs under different doping schemes, which can explain the change of the peak absorption coefficients. According to Eq. (3), peak absorption happens when  $E_2 - E_1 = hc/\lambda$ , meaning the peak absorption coefficient is proportional to  $|M_{12}|^2$  and  $n_{12}$ . The electron density of  $(20\bar{2}1)$  SQW under the QW doping scheme increases slightly when the doping concentration increases. In comparison, the other two doping schemes (i.e., barrier doping and  $\delta$ -doping) for  $(20\bar{2}1)$  SQW lead to a reduced  $n_{12}$  at high doping concentrations. This is due to the significant QW bowing under modulation doping schemes, which reduces the effective barrier height  $E_{B,eff}$  and results in lower subband energies. This result is further confirmed by different  $E_1$  and  $E_2$  under different doping schemes, which is shown in Figs. 5(c) and 5(d). For  $(20\bar{2}1)$  SQW under both  $\delta$ -doping and barrier doping schemes,  $E_2$  is much lower than the Fermi level than under the QW doping scheme, which means the second subband is more populated and decreases  $n_{12}$ . The scenario for  $(10\bar{1}3)$  SQW is different under all doping schemes, where  $n_2$  is much smaller than  $n_1$

and can be neglected. Therefore, an increase of  $n_1$  with a doping concentration explains larger  $n_{12}$  at a higher doping density. On the other hand,  $M_{12}$  of  $(20\bar{2}1)$  SQW drops with increasing doping concentrations under all doping schemes, while a small change was observed on  $M_{12}$  of  $(10\bar{1}3)$ . The distortion caused by QW bowing in  $(20\bar{2}1)$  SQW reduces the large wavefunction overlap of flat undoped QW profile. For  $(20\bar{2}1)$  SQW, the combination of reduced  $n_{12}$  and  $M_{12}$  gives rise to lower peak absorption coefficients at high doping concentrations under modulation doping schemes, while a combination of increased  $n_{12}$  and decreased  $M_{12}$  is observed for QW doping. Much higher  $n_{12}$  and relatively constant  $M_{12}$  are responsible for larger peak absorption coefficients at higher doping concentrations under all doping schemes for  $(10\bar{1}3)$  SQW.

## B. Spacer thickness in barrier doping

From the discussions above, barrier doping is promising for pushing the absorption to longer wavelength while

keeping the active region away from impurities. However, high doping concentrations could cause decreased absorption coefficients due to the large QW bowing. In addition to doping concentrations, another key aspect of the barrier doping scheme is the spacer thickness (which is set at 2 nm for the aforementioned discussions). Therefore, it is important to investigate how the spacer thickness will affect the ISBT properties with low doping concentrations. Here, (20 $\bar{2}$ 1) and (10 $\bar{1}$ 3) SQW with the same structure are studied with a donor concentration  $N_D$  of  $3 \times 10^{18} \text{ cm}^{-3}$  at varying spacer thicknesses from 0 nm to 10 nm. Note that 0 nm means there's no spacer layer in the structure, which is not ideal because of the interface scattering. Figure 6 shows the absorption spectra of (20 $\bar{2}$ 1) and (10 $\bar{1}$ 3) SQW with different spacer thicknesses under barrier doping scheme. For (20 $\bar{2}$ 1) structure, peak absorption coefficients increase, while the peak absorption wavelengths decrease, with increasing spacer thicknesses. For (10 $\bar{1}$ 3) structure, however, both peak absorption coefficients and wavelengths decrease when the thickness of the spacer layer increases.

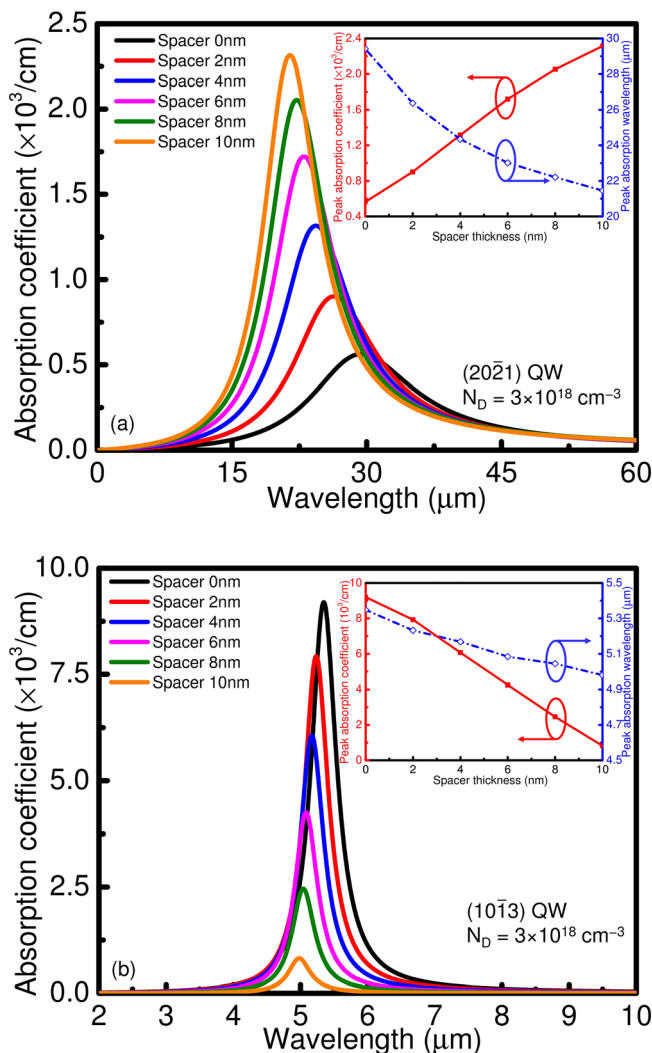


FIG. 6. Absorption spectra of (a) (20 $\bar{2}$ 1) QWs and (b) (10 $\bar{1}$ 3) QWs with spacer thickness ranging from 0 nm to 10 nm under the barrier doping scheme. The doping density is  $3 \times 10^{18} \text{ cm}^{-3}$ . The insets show the peak absorption coefficient and wavelength as a function of the spacer thickness.

Figures 7(a) and 7(b) present the subband electron density and  $M_{12}/e$  as a function of spacer thickness for (20 $\bar{2}$ 1) and (10 $\bar{1}$ 3) SQW. For (20 $\bar{2}$ 1) SQW, both  $n_1$  and  $n_2$  are reduced with large spacer thicknesses while  $n_{12}$  is almost constant. The reduction of  $n_1$  and  $n_2$  is due to the induced electron concentration in the QW, which is proportional to the distance between the barrier donor charge and QW. Increasing spacer thicknesses will move the doped layer farther from the QW, causing a less induced charge in the QW. On the other hand,  $M_{12}$  increases rapidly with increasing spacer thickness due to less QW bowing and thus more wavefunction overlap as shown in Figs. 7(c) and 7(d). The peak absorption coefficient of (20 $\bar{2}$ 1) SQW becomes larger with thicker spacer since the peak absorption coefficient is proportional to  $M_{12}$  squared and  $n_{12}$  according to Eq. (3). For (10 $\bar{1}$ 3) SQW, completely different tendencies are observed:  $n_2$  is negligible, and  $n_1$  is reduced with increasing spacer thickness, which gives a smaller  $n_{12}$ . This behavior of  $n_{12}$  variation stems from the fact that  $E_2$  is above or close to the Fermi level, and  $n_2$  is insignificant. Furthermore,  $M_{12}$  is also decreasing with the spacer thickness. Therefore, (10 $\bar{1}$ 3) device is observed with a smaller peak absorption coefficients with thicker spacer layers. As far as the change of peak absorption wavelength, it can be analyzed through the bandstructure and subband wavefunction that are calculated in Figs. 7(c)–7(f). (20 $\bar{2}$ 1) SQW with 8 nm thick spacer has a relatively less bowing in the QW and a larger subband wavefunction overlap. The former result makes  $E_{B,eff}$  larger that results in the larger energy separation of first two subbands, i.e., shorter peak absorption wavelength. The latter results is the reason for increased  $M_{12}$  with a thicker spacer. With 8 nm spacer, (10 $\bar{1}$ 3) SQW shows a larger negative slope in the QW creating a deeper triangular potential, which further separates  $E_1$  and  $E_2$  meaning a smaller peak absorption wavelength. In addition, no significant change of subband wavefunction overlap is observed when including the thick spacer layer.

### C. Position of delta doping

Besides the barrier doping scheme, the other modulation doping scheme, i.e.,  $\delta$ -doping, shows some advantages since a very high  $\delta$ -doping can be achieved without degrading the material quality and needs much less dopants.<sup>13</sup> In addition to the doping concentrations, the positions of the  $\delta$ -doping also have significant impacts on the ISBT properties of the SQW structures. Figures 8(a) and 8(b) present the absorption spectra of (20 $\bar{2}$ 1) and (10 $\bar{1}$ 3) SQW with various  $\delta$ -doping locations in the barrier, where the doping concentration is kept at  $4 \times 10^{12} \text{ cm}^{-2}$  for the simulation. The peak absorption coefficient of (20 $\bar{2}$ 1) SQW becomes larger and the peak absorption wavelength smaller as the  $\delta$ -doping is moving away from the QW layer. (10 $\bar{1}$ 3) structures have both decreased peak absorption coefficients and wavelengths with increasing  $\delta$ -doping position. In Fig. 8(c), it is observed that for (20 $\bar{2}$ 1) SQW,  $n_{12}$  is almost constant while the  $M_{12}$  increases with increasing  $\delta$ -doping position. This could account for the large peak absorption coefficients observed on (20 $\bar{2}$ 1) SQW. In Fig. 8(d), it is shown that (10 $\bar{1}$ 3) SQW

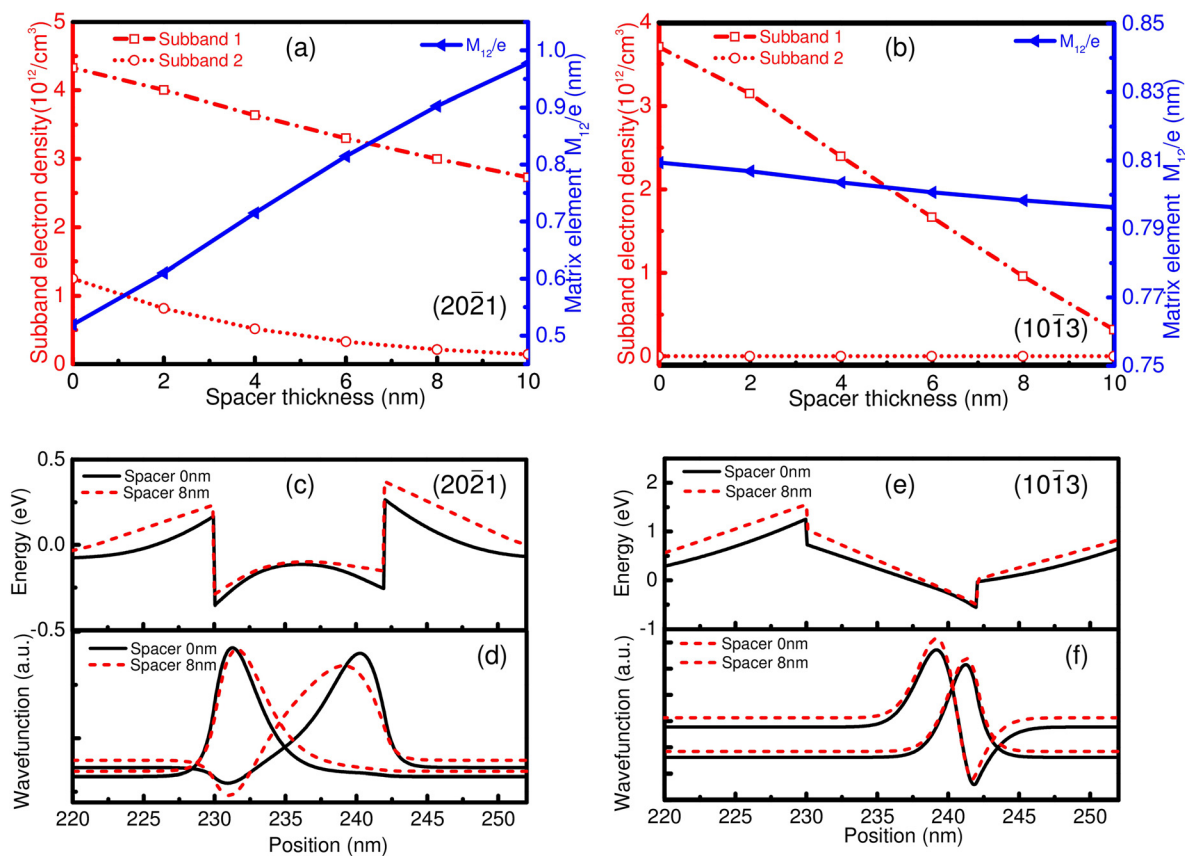


FIG. 7. The electron density of first two subbands and the matrix element  $M_{21}/e$  versus spacer thickness for (a)  $(20\bar{2}1)$  QWs and (b)  $(10\bar{1}3)$  QWs. (c)–(f) conduction band and electron wavefunctions of first two subbands of  $(20\bar{2}1)$  QWs (c) and (d) and  $(10\bar{1}3)$  QWs (e) and (f) with/without the spacer layer.

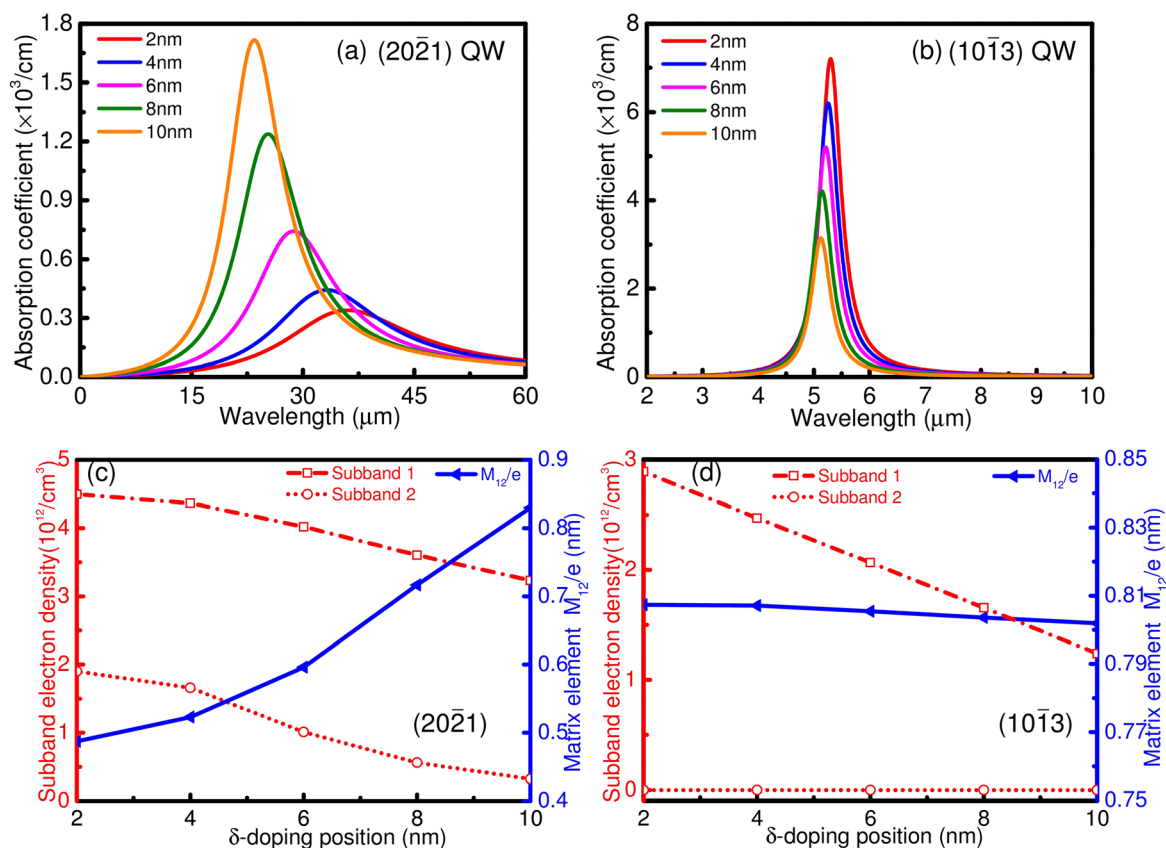


FIG. 8. Absorption spectra of (a)  $(20\bar{2}1)$  QWs and (b)  $(10\bar{1}3)$  QWs with different  $\delta$ -doping positions. Subband electron density and matrix element  $M_{21}/e$  as a function of the  $\delta$ -doping position for (c)  $(20\bar{2}1)$  QWs and (d)  $(10\bar{1}3)$  QWs.

exhibits almost constant values for  $M_{12}$  with different  $\delta$ -doping positions, while the  $n_{12}$  decreases with the doping position, which leads to the smaller peak absorption coefficients in the (10 $\bar{1}$ 3) SQW at large  $\delta$ -doping positions. The change of peak absorption wavelengths is also related to the QW bowing as discussed in the barrier doping scheme. Although changing the location of barrier doping and  $\delta$ -doping has a similar influence on the ISBT properties for (20 $\bar{2}$ 1) and (10 $\bar{1}$ 3) SQW, it is worthy to mention that  $\delta$ -doping is more efficient in realizing a longer absorption wavelength than barrier doping due to stronger impacts on the QW profiles. This is because the centroid of the donor charge in  $\delta$ -doping is closer to the QW than that of barrier doping when the distance between the edge of barrier donor and QW is the same. All these results indicate that  $\delta$ -doping is preferable to barrier doping if the modulation doping is being used.

#### IV. CONCLUSIONS

We study the ISBT properties of (20 $\bar{2}$ 1) and (10 $\bar{1}$ 3) AlGaIn/GaN SQW under modulation schemes (i.e., barrier continuous doping and  $\delta$ -doping.) at 150 K. (20 $\bar{2}$ 1) SQW has decreased peak absorption coefficients and increased peak absorption wavelengths at high doping concentrations (e.g.,  $>5 \times 10^{18}$ – $10^{19}$  cm $^{-3}$ ) due to large bowing in the flat QW profile, while the (10 $\bar{1}$ 3) SQW is less affected by doping concentrations due to tilted QW profiles. Moreover, the effect of modulation doping is highly dependent on the locations of donor charge. Increasing the spacer thickness in barrier continuous doping scheme or moving the  $\delta$ -doping away from the QW in barrier  $\delta$ -doping scheme alleviates the band bowing of the QW profile, resulting in a higher peak absorption coefficient and a smaller peak absorption wavelength. Compared to the barrier continuous doping scheme, barrier  $\delta$ -doping scheme can dope the QW and modify the QW profile more effectively due to the closer position of dopants relative to the active region.

#### ACKNOWLEDGMENTS

This work is supported by Bisgrove Scholar program from the Science Foundation, Arizona.

<sup>1</sup>S. Nakamura, G. Fasol, and S. J. Pearton, *The Blue Laser Diode: The Complete Story*, 2nd ed. (Springer, 2000).

<sup>2</sup>S. Nakamura, T. Mukai, and M. Senoh, *Appl. Phys. Lett.* **64**, 1687 (1994).

<sup>3</sup>Y. Zhao, J. Sonoda, I. Koslow, C. C. Pan, H. Ohta, J. S. Ha, S. P. DenBaars, and S. Nakamura, *Jpn. J. Appl. Phys.* **49**, 070206 (2010).

<sup>4</sup>Y. Zhao, S. H. Oh, F. Wu, Y. Kawaguchi, S. Tanaka, K. Fujito, J. S. Speck, S. P. DenBaars, and S. Nakamura, *Appl. Phys. Express* **6**, 062102 (2013).

<sup>5</sup>E. Bellotti, K. Driscoll, T. Moustakas, and R. Paiella, *Appl. Phys. Lett.* **92**, 101112 (2008).

<sup>6</sup>D. Feezell, Y. Sharma, and S. Krishna, *J. Appl. Phys.* **113**, 133103 (2013).

<sup>7</sup>D. Hofstetter, S. Schad, H. Wu, W. Schaff, and L. Eastman, *Appl. Phys. Lett.* **83**, 572 (2003).

<sup>8</sup>S. Sakr, E. Giraud, A. Dussaigne, M. Tchernycheva, N. Grandjean, and F. Julien, *Appl. Phys. Lett.* **100**, 181103 (2012).

<sup>9</sup>H. Schneider and H. Liu, *Quantum Well Infrared Photodetectors: Physics and Applications* (Springer, Berlin, 2006).

<sup>10</sup>A. Helman, M. Tchernycheva, A. Lussion, E. Warde, F. H. Julien, Kh. Moutamanis, G. Fishman, E. Monroy, B. Daudin, D. Le Si Dang, E. Bellet-Amalric, and D. Jalabert, *Appl. Phys. Lett.* **83**, 5196 (2003).

<sup>11</sup>P. K. Kandaswamy, H. Machhadani, Y. Kotsar, S. Sakr, A. Das, M. Tchernycheva, L. Rapenne, E. Sarigiannidou, F. H. Julien, and E. Monroy, *Appl. Phys. Lett.* **96**, 141903 (2010).

<sup>12</sup>T. Kotani, M. Arita, and Y. Arakawa, *Appl. Phys. Lett.* **107**, 112107 (2015).

<sup>13</sup>C. Edmunda, L. Tang, J. Shao, D. Li, M. Cervantes, G. Gardner, D. N. Zakharov, M. J. Manfra, and O. Malis, *Appl. Phys. Lett.* **101**, 102104 (2012).

<sup>14</sup>C. Edmunds, J. Shao, M. Shirazi-HD, M. J. Manfra, and O. Malis, *Appl. Phys. Lett.* **105**, 021109 (2014).

<sup>15</sup>T. Kotani, M. Arita, and Y. Arakawa, *Appl. Phys. Lett.* **105**, 261108 (2014).

<sup>16</sup>H. Machhadani, M. Beeler, S. Sakr, E. Warde, Y. Kotsar, M. Tchernycheva, M. P. Chauvat, P. Ruterana, G. Nataf, Ph. De. Mierry, E. Monroy, and F. H. Julien, *J. Appl. Phys.* **113**, 143109 (2013).

<sup>17</sup>L. Lahourcade, P. K. Kandaswamy, J. Renard, P. Ruterana, H. Machhadani, M. Tchernycheva, F. H. Julien, B. Gayral, and E. Monroy, *Appl. Phys. Lett.* **93**, 111906 (2008).

<sup>18</sup>H. Fu, Z. Lu, X. Huang, H. Chen, and Y. Zhao, *J. Appl. Phys.* **119**, 174502 (2016).

<sup>19</sup>C. Gmachl, H. M. Ng, and A. Y. Cho, *Appl. Phys. Lett.* **77**, 334 (2000).

<sup>20</sup>N. Iizuka, K. Kaneko, and N. Suzuki, *Appl. Phys. Lett.* **81**, 1803 (2002).

<sup>21</sup>A. Romanov, T. Baker, S. Nakamura, and J. Speck, *J. Appl. Phys.* **100**, 023522 (2006).

<sup>22</sup>H. Chen, H. Fu, Z. Lu, X. Huang, and Y. Zhao, *Opt. Express* **24**, A856 (2016).

<sup>23</sup>C. C. Pan, S. Tanaka, F. Wu, Y. Zhao, J. S. Speck, S. Nakamura, S. P. DenBaars, and D. Feezell, *Appl. Phys. Express* **5**, 062103 (2012).

<sup>24</sup>C. C. Pan, Q. Yan, H. Fu, Y. Zhao, Y. R. Wu, C. G. Van de Walle, S. Nakamura, and S. P. DenBaars, *Electron. Lett.* **51**, 1187 (2015).

<sup>25</sup>H. Fu, Z. Lu, X. Zhao, Y. Zhang, S. P. DenBaars, S. Nakamura, and Y. Zhao, *J. Disp. Technol.* **12**, 736 (2016).

<sup>26</sup>X. Huang, H. Fu, H. Chen, Z. Lu, D. Ding, and Y. Zhao, *J. Appl. Phys.* **119**, 213101 (2016).

<sup>27</sup>H. Fu, Z. Lu, and Y. Zhao, *AIP Adv.* **6**, 065013 (2016).

<sup>28</sup>H. Durmaz, D. Nothorn, G. Brummer, T. D. Moustakas, and R. Paiella, *Appl. Phys. Lett.* **108**, 201102 (2016).

<sup>29</sup>V. F. Mymrin, K. A. Bulashevich, N. I. Podolskaya, I. A. Zhmakin, S. Yu. Karpov, and Yu. N. Makarov, *Phys. Status Solidi C* **2**, 2928 (2005).

<sup>30</sup>See <http://www.str-soft.com/products/SiLENSe/> for more information about SiLENSe.

<sup>31</sup>Y. Zhao, R. M. Farrell, Y. R. Wu, and J. S. Speck, *Jpn. J. Appl. Phys. Sel. Top. Appl. Phys.* **53**, 100206 (2014).

<sup>32</sup>D. Ahn and S. Chuang, *IEEE J. Quantum Electron.* **23**, 2196 (1987).